

Getting nanometric MoO₃ through chemical synthesis and high energy milling

M. Santos-Beltrán, F. Paraguay-Delgado, A. Santos-Beltrán, L. Fuentes

Abstract

The effects of high energy mechanical milling (HEMM) were studied on the microstructure and optical properties of MoO₃ for hexagonal and orthorhombic phases. Employing HEMM was possible change particle size as a function of mechanical milling time, as well as the small quantity transformation percentage from hexagonal to orthorhombic phase. The relationship between microstrain and optical properties generated was studied. The electronic structures were calculated using the Density Functional Theory (DFT); to determinate partial density of state (PDOS). Band gap structure calculations show a good correlation between experimental and simulated data. The approximated values of microstrain, particle size, lattice parameters and oxygen vacancies were obtained employing the Rietveld refinement of X-ray diffraction patterns. Samples were characterized by electron microscopy techniques, surface area analysis (BET), thermal-gravimetric analysis (TGA), differential scanning calorimetry (DSC) and ultraviolet-visible spectroscopy (UVeVis). It was possible, obtain particles with size below 40 nm by 30 min milling.

Introduction

Molybdenum trioxide (MoO_3), is an attractive material for its different applications for new technologies as: field emission de-vices [1], lithium-ion battery electrodes [2], electrochromic sur-faces [3], gas sensors [4], and as a catalyst in the hydrodesulfurization (HDS) process [5]. This material can be synthesized by sol-gel [6], microwave-assisted hydrothermal process [7], sonochemical [8], and also through hydrothermal treatments [5, 9, 10]. Many physical properties of the materials depend significantly on their size, shape and crystalline structure. Because of this characteristics, the material science has been focused on the nanometric size materials. HEMM is an adequate technique for reducing the size of MoO_3 particles [11], or generate mesoporous and macroporous [12]. The reduced particle dimensions achieved by this mechanism is due to the interactions among them during the intense mechanical interactions. This process also generates the formation of several defects [13]. Thus, deformed structures, such as point defects (oxygen vacancies) could be generate mechanical stress and changes in the optical properties of the material. Besides decreasing crystallite sizes and deforming the particle morphologies, the interatomic distances and therefore lattice symmetries may be affected. On the other hand due to the particles broken could be generate active sites on the material's surface, useful for catalytic applications and other [14,15].

In this work, the micrometric size material was synthesized by hydrothermal method. Subsequently, through mechanical milling, the particle size was reduced to nanometric dimensions in a short time. The MoO_3 properties were studied as a

function of milling time for orthorhombic and hexagonal crystalline phases.

2. Experimental

2.1. Chemicals

Ammonium heptamolybdate tetrahydrate ((NH₄)₆Mo₇O₂₄·4H₂O) and nitric acid (HNO₃, 70 wt. %) were purchased from Sigma-Aldrich.

2.2. Synthesis

Micrometric size molybdenum oxide particles with hexagonal and orthorhombic crystalline structures were synthesized using the hydrothermal method [5].

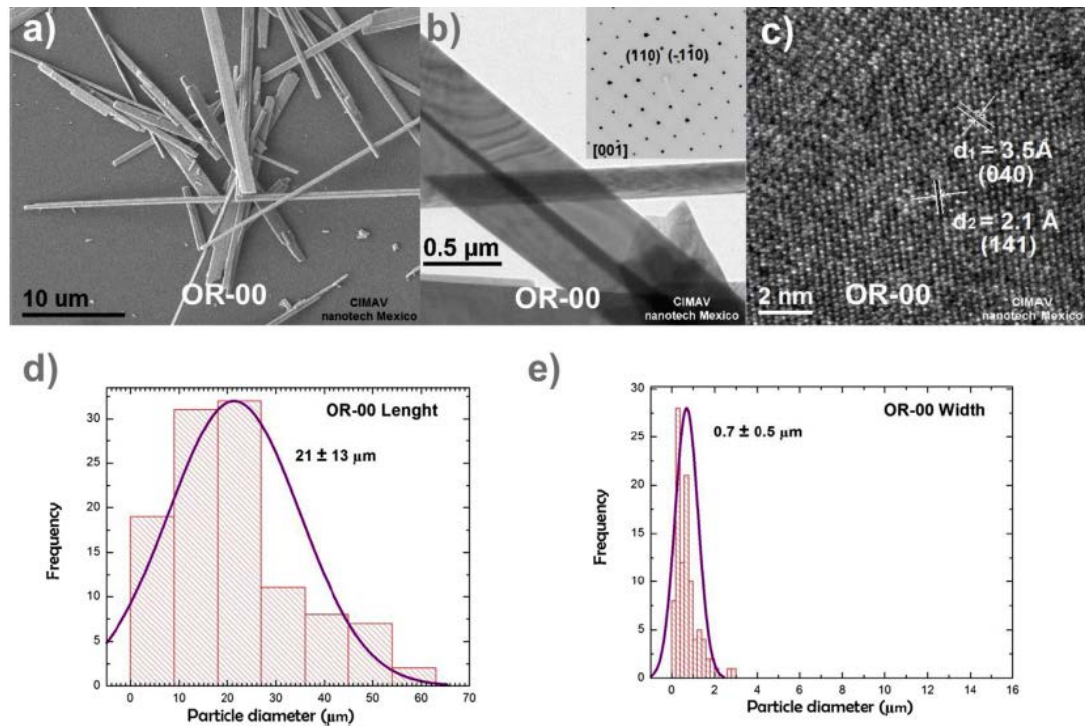


Fig. 1. Orthorhombic phase particles morphology before milling. a) SEM image, b) TEM image and SAED pattern, c) TEM image at higher magnification, d) and e) length and width statistical distribution.

The synthesis was carried out from an aqueous precursor solution of ammonium heptamolybdate at 0.3 M; the pH was adjusted at 5 using 2.2 N nitric acid. In order to synthesize the orthorhombic phase, the precursor solution was previously aged for 5 days within a tightly sealed flask and kept under constant stirring at 60 °C. Afterwards, 5 mL of this solution were mixed with 5 mL of tri-distilled water and add 5 mL of nitric acid (2.2 N). This mixture was placed in a stainless steel autoclave

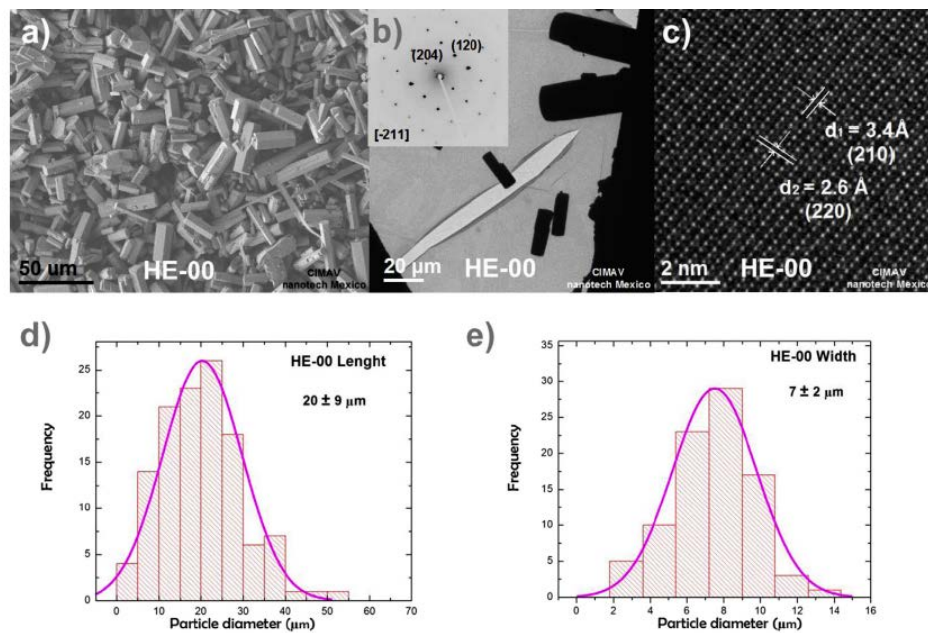


Fig. 2. Hexagonal phase particles morphology before milling. a) SEM image, b) TEM image and SAED pattern, c) TEM image at higher magnification, d) and e) length and width statistical distribution.

equipped with a Teflon vial and it was submitted to hydrothermal treatment at 200 °C for 36 h. The resulting material was collected by centrifugation for 3 times, each time was washed with de-ionized water and finally the powders were dried for 5 h at 90 °C. For the synthesis of the hexagonal phase, the same amount of reagents were used and it was follow the same procedure, but in this case the starting solution has not ageing process.

2.3. Characterizations

The high-energy milling process was carried out in dry conditions at room temperature in a stainless-steel vial using Zirconia dioxide spheres with 1 cm diameter and 1 g weight. The equipment used was a high-energy mill model SPEX 8000, it was conditioned to set different milling cycles (0.5, 2 and 6 h). In the milling process the weight ratio of spheres to material was kept at 5:1 always. The microstructural analysis of the samples was studied by X-ray diffraction (XRD) using a Philips X'Pert MPD diffractometer with Cu K α 1 radiation ($\lambda = 1.54056 \text{ \AA}$) operating at 40 kV and a current of 30 mA. Particle morphology was studied by scanning electron microscopy (SEM) using a JSM-7401F field emission microscope operated at 5 kV and 17 kV, first one for acquire images and second for elemental analysis. Transmission electron microscopy (TEM) was carried out using a Jeol JEM-2200FS microscope operating at 200 kV. The samples for TEM study were dispersed in methanol by sonication and one drop of it was deposited onto a lacy carbon film on a copper grid. Surface area analysis (BET) was performed using an Autosorb-1 equipment (Quanta Crome) the samples were degassed at 150-250 °C for 12 h before the measurement procedure, thermal gravimetric (TG) and differential thermal gravimetric analysis (TGA) were performed in a simultaneous equipment Q600 TA Instruments using a 10 °C/min heating rate from room temperature to 900 °C. Optical properties were studied in the UV-visible range by diffuse reflectance spectroscopy in a Lambda 10 spectrophotometer (PerkineElmer), IR spectra was acquired by Spectrum Gx FT-IR system (PerkineElmer), using ATR reflectance with diamond window, the resolution was 4 cm^{-1} . Microstructural parameters were assessed by X-ray diffraction pattern refinement using the Rietveld method in a

Fullprof free software. The values determined by this analysis were used to carry out the simulation, using the framework of Density Functional Theory (DFT) employing generalized gradient approximation (GGA). The MoO₃ electronic structure was calculated for both

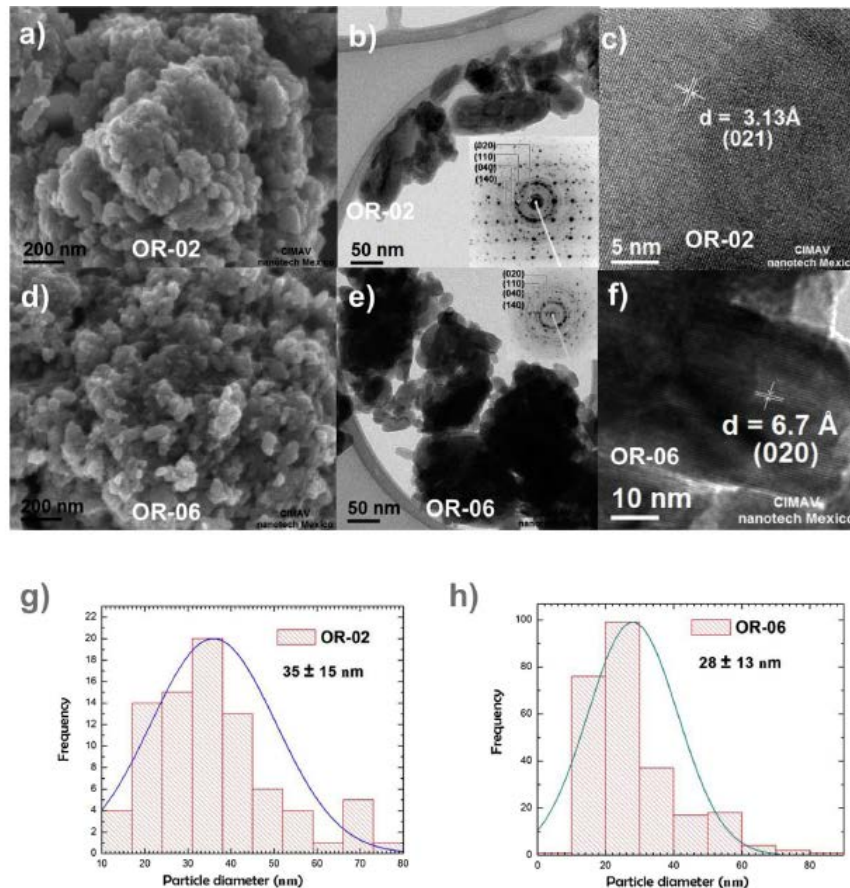


Fig. 3. Orthorhombic phase particles morphology after 2 and 6 h of milling. a) and d) SEM images, b) and e) TEM images and SAED patterns, c) and f) d-spaces at higher magnification TEM image, g) and h) diameter size statistical distribution.

crystalline structures, before and after the milling process. The samples names nomenclature were assigned as OR-00 and HE-00 for orthorhombic and hexagonal phase without milling, respectively. In the case of milling samples it was ad the milling time, for example being OR-02 and HE-02 for 2 h milling samples.

3. Results

3.1. Morphology previous to the milling process

The morphologies of the synthesized particles were studied by SEM and TEM images. Both, length and diameter were measured for each particle. Figs. 1a and 2a show SEM micrographs obtained by secondary electrons for orthorhombic and hexagonal phases, respectively. All particles show uniform and smooth surface. The morphology of the OR-00 sample reveals that their geometrical shape is elongated ribbon-like particle with an average length and width of 21 ± 13 and 0.7 ± 0.5 mm, respectively and approximately 0.1 mm thickness. Regarding the HE-00 material, the particles are elongated and hexagonal prism-like shaped with an average diameter and length of 7 ± 2 and 20 ± 9 mm, respectively. Particle images for both samples (OR-00 and HE-00) by TEM using the bright field mode image are depicted in Figs. 1b and 2b. These images confirm the ribbon and hexagon morphology of the orthorhombic and hexagonal phases, respectively. The selected area electron diffraction (SAED) patterns included in each one of these images, show the particles are monocrystalline; these SAED patterns shows the orthorhombic and hexagonal phases, the zone axis are $[001]$ and $[-211]$, respectively. Figs. 1c and 2c show images at higher magnification. It can be notice there the interlayer distances, thus confirming the particle's mono crystallinity by displaying the atomic array lattice images for both phases. For the HE-00 sample, the image was acquired from chipped edges because these particles has higher thickness to be completely visualized by TEM. Figs. 1d and 2d show the statistical distribution of the particle's length. Both graphs show that it is about 20 mm. Regarding the particle's width or

diameter, the statistical distribution is around 0.7 and 7 μm (Figs. 1e and 2e) for orthorhombic and hexagonal phase. The particles dimension as synthesized by hydrothermal method are within the micrometer range.

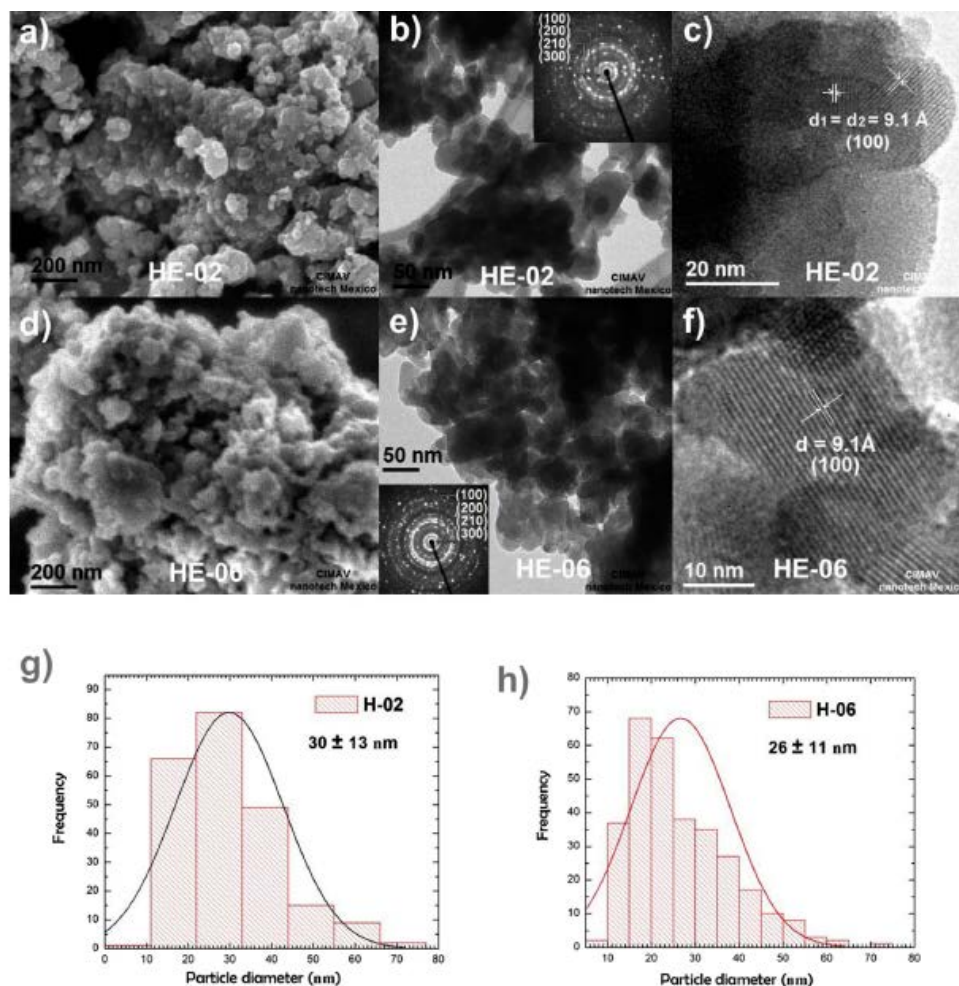


Fig. 4. Hexagonal phase particles morphology after 2 and 6 h of milling. a) and d) SEM images, b) and e) TEM images and SAED patterns, c) and f) d-spaces at higher magnification TEM image, g) and h) diameter size statistical distribution.

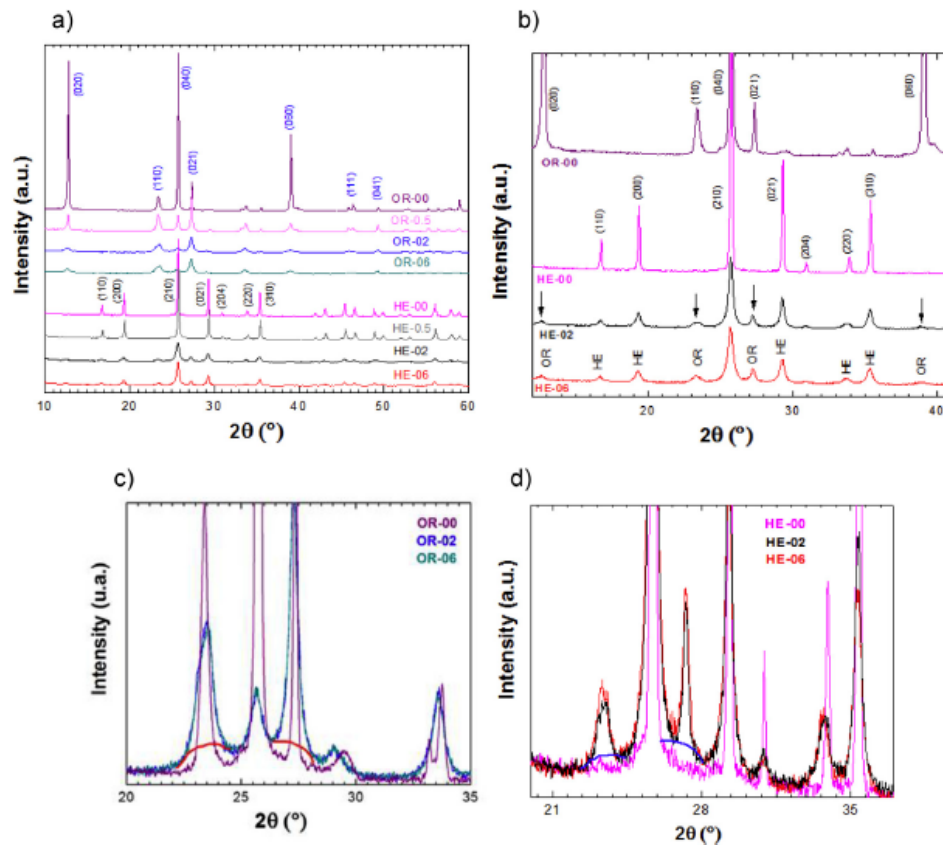


Fig. 5. XRD patterns comparison as a function of a) milling time, b) phase transformation for 2 and 6 h. Then patterns overlapping to quantify amorphous phase for c) orthorhombic phase and d) hexagonal phase.

3.2. Morphology changes by milling process

Fig. 3 shows, the morphological changes induced on the orthorhombic phase after 2 and 6 h of milling. Fig. 3a, b and c, show the images acquired after a 2 h milling, whereas Fig. 3d, e and f depict the sample after 6 h of milling. The shape of these particles is slightly elongated and equiaxial ('spherical'). The images from the particle acquired at high magnification (Fig. 3d and f) still show crystallinity, based on the visualization of the lattice distances and the Moire bands. The SAED patterns are typical of a polycrystalline material with some symmetrical intense directions. It is appreciated, higher amount of diffracted electrons of which intensities make up a

symmetry after a 2 h milling. When the material is submitted to a longer time milling (6 h) the intensities make up close to circles, indicating a further decrease of crystallite size. Fig. 3g and h shows the statistic distribution of particle diameter measurements after both milling periods. The particle size decreased is clearly appreciated, being the average diameter 35 ± 15 nm and 28 ± 13 nm after 2 and 6 h of milling, respectively. Fig. 4 contains the images that show the morphological changes for the hexagonal phase after 2 and 6 h of milling. These images also represent the decrease in particle size. Each one of these maintains their crystallinity, as shown in Fig. 4c and f, in which the interlayer distances and the Moire bands are clearly appreciated. Additionally, the HE-06 sample displays an improved circles shape pattern definition in the SAED, indicating a further decrease in crystal size. The particle size distribution is shown in Fig. 4g and h. In both cases, the size decreases reaching 30 ± 13 nm and 26 ± 11 nm after 2 and 6 h of milling, respectively. The SAED patterns for these milling times do not show any symmetrical array intensities, they are circular shape in both cases, resulting in nanometric poly-crystalline material.

3.3. Structural changes caused by milling

The influence on the crystalline structure was studied using XRD patterns as a function of milling time. The diffraction peaks are significantly broadened for both phases, due to the combined effect of decreasing crystallite size and/or the presence of microstrain and possible defects. Regarding to the particle size, it correlates well with the nanocrystalline state previously observed in the acquired micrographs (Figs. 3 and 4). The XRD patterns were studied by performing a

refinement analysis (Rietveld method). In contrast, it is observed an evident decrease of peak intensities due to particle size decrease. Fig. 5a shows an XRD comparison between both phases. The four diffraction patterns shown in the upper part are from the orthorhombic phase (space group 62 Pbnm JCPDS 05-0508), this phase displays an stacking layers, being this d-spaces family indexed by (0k0) miller index, with an even k number ($k = 2n$, n integer). These layers interact each other through the Van der Waals forces [16, 17]. It is observed that the (0k0) peak intensity systematically decreases with the milling time, being this

Table 1
Lattice parameters summary and atomic positions before and after milling, obtained from XRD Rietveld refinement.

Lattice parameters (Å) Orthorhombic phase													
Reference JCPDS 05-0508				OR-00			OR-02			OR-06			
a	3.96			3.96			3.96			3.95			
b	13.85			13.84			13.92			13.93			
c	3.69			3.69			3.72			3.72			
Change %				0			0.6			0.9			
X ²				22			7			6			
Atomic positions													
Atm.	x	y	z	x	y	z	x	y	z	x	y	z	z
Mo	0.086	0.101	0.25	0.062	0.101	0.25	0.065	0.101	0.25	0.062	0.101	0.25	0.25
O	0.499	0.435	0.25	0.483	0.442	0.25	0.500	0.442	0.25	0.483	0.442	0.25	0.25
O	0.521	0.086	0.25	0.554	0.097	0.25	0.528	0.097	0.25	0.554	0.097	0.25	0.25
O	0.037	0.221	0.25	0.072	0.221	0.25	0.087	0.221	0.25	0.072	0.221	0.25	0.25
Lattice parameters (Å) Hexagonal phase													
Reference JCPDS-21-0569				HE-00			HE-02			HE-06			
a = b	10.53			10.56			10.58			10.58			
c	3.728			3.72			3.72			3.72			
Change %				0			0.2			0.3			
X ²				4.5			4.0			3.1			

Plane more sensitive to mechanical milling. The interpretation is that this layers is easier to break or cleave in this direction due to the weak interaction bonding [18]. In the case of the hexagonal phase, the four diffract grams located at the bottom part of Fig. 5a, show the patterns for different milling times. The XRD patterns show the characteristic peaks belongs to this phase (space group 176 P63/M JCPDS-21-0569). A phase change from hexagonal to orthorhombic phase is

observed on the XRD patterns showed (zoom in Fig. 5b), the new diffraction peaks were labelled by arrows. The percentage of this phase was assessed by Rietveld refinement being between 7 and 13% for 2 and 6 h milling time, respectively. The amounts are in accordance and it was correlate between the milling times and the amount generated percentage. This is the major reason why it is not convenient to carry out a milling for more than 2 h, i.e. to avoid the presence of orthorhombic phase by milling from the hexagonal phase.

Fig. 5c and d shows the XRD patterns superimposed in order to identify the increase of the amorphous phase as a consequence of the milling process. A slight increase of the amorphous curve is observed regarding to the base line, which leads to particle amorphisation [19]. But in this case, small quantity became to this phase, most of the particles preserve their original crystallinity (hexagonal). In order to calculate the amorphisation quantity percentage, the integrated area of the selected section (2θ between 21° and 30°) was defined. Subsequently, the area of the amorphous shape was calculated as shown in Fig. 5c and d for both type of phases. The quantification was made using the following Equation (1) [20].

$$\%Crystallinity = \frac{\text{Area of crystalline peaks}}{\text{Area of crystalline peaks} + \text{amorphous shape}}$$

$$\%Amorphisation = 100 - \%Crystallinity$$

The amount of amorphisation was around, 5.2% for the orthorhombic phase and 4.3% for the hexagonal phase, this values were determined for samples after 6 h of milling.

3.4. Parameter assessment by rietveld refinement method

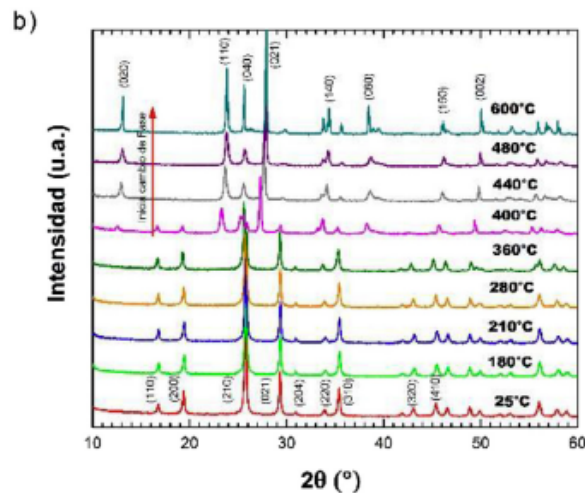
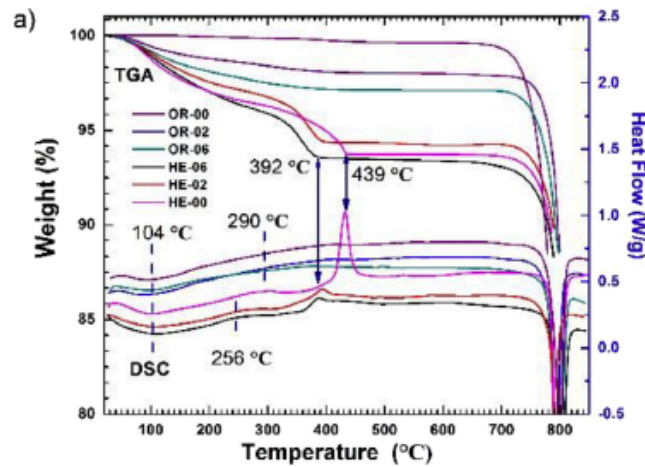
The XRD patterns were refined in order to determine variations in particle size, lattice parameters, oxygen vacancies and micro-strain. The numerical data is shown in Tables 1 and 2. Table 1 shows the lattice parameter variation using cards from (JCPDS 05-0508

Table 2

Particle size average measurements values, from images and XRD refinement, microstrain, oxygen vacancy, percentage phase change and amorphisation.

Samples	Particle size from:		Rietveld refinement (nm)	Microstrain (%) $\times 10^{-4}$	Oxygen vacancy (%)	Phase change HE to OR (%)	Amorphisation (%)
	SEM images (μm)						
	L	W					
OR-00	21 \pm 13	0.7 \pm 0.5	143 ^T	14.6	0		
OR-0.5			39	14.2	0		
OR-02		35 \pm 15	28	147.1	3.9		
OR-06		28 \pm 13	26	140.1	6.5		5.2
HE-00	20 \pm 9	7 \pm 2	—	4.6	0		
HE-0.5			48	8.5	0		
HE-02		30 \pm 13	22	28.8	1.2	7	
HE-06		26 \pm 11	18	31.1	1.9	13	4.3

L: Length; W: Width; T: Thickness.



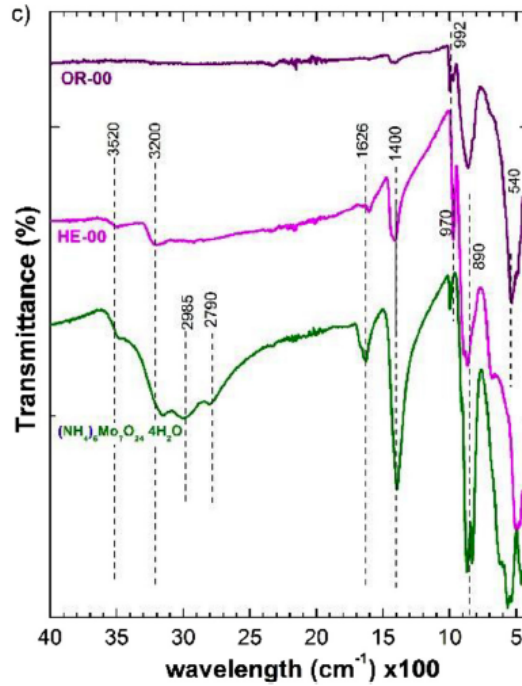


Fig. 6. Changes by heat treatment a) Thermogravimetric analysis, b) XRD Patterns acquire by insitu heating the HE-02 sample and c) IR functional group analysis.

And JCPDS-21-0569) as references for the orthorhombic and hexagonal phases, respectively. The lattice parameters values show a variation of 0.6 and 0.3% for the orthorhombic and hexagonal phases. This slight variation of the unit cell is due to the presence of microstrain within the crystal [21]. The atomic positions were refined only for the orthorhombic phase, with slight changes. In the case of hexagonal phase the atomic positions was remain from the reference (JCPDS-21-0569). The statistical precision (or correlation) of the XRD patterns refinement was assessed with χ^2 (chi2) employing Equation (2).

$$\chi^2 = \sum_i \frac{W_i (y_i - y_{ci})^2}{(N - M)}$$

Where:

y_i = experimental intensities of the diffraction pattern

y_{ci} = contributions of all diffraction peaks to the considered angle.

y_c = calculated intensities of the diffraction pattern.

W_i = respective weights at these intensities. Generally the criteria $W_i = 1/y_i$ is used.

N = number of points measured within the pattern

M = amount of refined parameters.

These x^2 values were around 7, except for the sample OR-00 which was around 22. In general, the materials do not undergo drastic changes after the milling process, the structural parameters remains as a consequence to the milling process for this type of materials, the results confirm about this method as a good method to obtaining nanometric size of MoO_3 .

The first three column of Table 2 shows the particle size measurements made from the SEM and TEM micrographs in comparison with determined by Reitveld refinement. The measurement from SEM images (first column) are in micron scale for samples without milling, the next two columns are in the nanometer scale, values measurement by TEM and refinement. This table shows those crystallite size results less than 50 nm for samples after the milling process. In general, there are an evident correlation between milling time and particle size decrease. It can be notice a drastic diminished crystallite size (less to 40 nm) with short milling times (half hour) for both phases (samples OR-0.5 and HE-0.5). By inspecting the values, it is apparent that the size does not further decrease by extending the milling time more than 2 h. This table also shows the microtension values generate by milling process, these values are very low. It confirming a milling time, less than 2 h for MoO_3 can be

obtain nanoparticles without drastically altering the material structure.

3.5. Thermal stability

The materials after milling were studied by thermal-gravimetric and differential thermal-gravimetric analysis, in order to assess changes on their thermal stability.

The TGA and DSC graphs for as synthesized and milling materials are presented in Fig. 6a, the hexagonal phase sample without mechanical milling show an exothermic reaction at 439 °C, thus confirming the transformation to the orthorhombic phase.

However, when the same hexagonal phase is submitted to mechanical milling for 2 and 6 h, they show an exothermic peak at 392 °C for the phase transition. Due to the milling process, the phase change occurs approximately 50 °C lower in comparison with the material without milling. This is as a consequence of particle size

(nanometric). In order to confirm this finding, the XRD patterns was acquired as a function of the

Table 3
Thermogravimetric analysis for samples before and after milling.

TG analysis	Temp. °C	Weight loss %					
		HE-00	HE-02	HE-06	OR-00	OR-02	OR-06
Dehydration	55–150	2.29	1.28	2.13	0	0.99	1.48
Deammonization	200–360	3.99	3.62	4.57			
Phase Change	400–460	6.31					
	360–420		5.6				
	355–405			6.48			
Total weight loss (%)		6.32	5.67	6.38	0.46	2.02	2.94

Temperature by performing in situ heating inside the X-ray diffractometer employing temperature ramps from 25 °C to 600°C from the hexagonal phase material after 2 h milling. These results are shown in Fig. 6b, it confirming the phase change around 400 °C. This pattern evolution confirm this temperature phase change, this is due to the heating transfer is better for nanometric size particles.

Regarding for the orthorhombic phase, there are no phase changes, it shows good

stability before and after the milling. The weight loss percentage and temperature ranges for dehydration, deammonization and phase transformation are summarized in Table 3. The first weight loss around 104 °C (clear on DSC) is due to the complete desorption of remain water molecules that are physically adsorbed on the surface of material. The second weight loss between 256 and 290 °C (for HE-02, HE-06 and HE-00) it is due to the remaining ammonia (NH₄) from the MoO₃ sample after dehydration and deammonization process. The sudden weight loss (TG) and rise of sharp exothermic peak (DSC) in the range from 350 to 450 °C for hexagonal phase samples is due to the atoms rearrange sample for phase change from hexagonal to orthorhombic structure. The last strong mass loss, which start around 785 °C is due to the MoO₃ fusion and decomposition. These values are in accordance with the results observed by A. Chithambararaj et al. [22].

Fig. 6c shows a transmittance IR vibrational Spectra for samples HE-00, OR-00 and precursor ammonium heptamolybdate ((NH₄)₆ Mo₇O₂₄·4H₂O) salt. In the spectral range of wavenumber 400-4000 cm^{-1} . The peaks at 3520 cm^{-1} and 1626 cm^{-1} correspond to the stretching and bending vibration of water molecules, due to the eOH group. The wide signal between 3400 and 2600 cm^{-1} and sharp peak localized at 1400 cm^{-1} are due to stretching and bending vibration of NeH from NH₄⁺ ammonia groups. It can be noticed, in the orthorhombic phase (OR-00) that

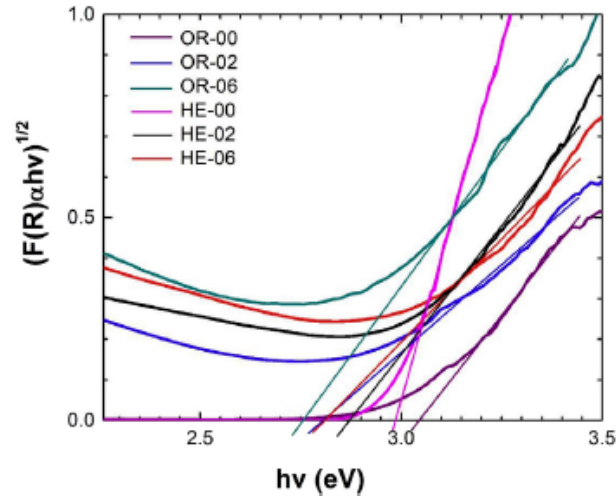


Fig. 7. Kubelka-Munk graphic to calculate the band gap energy for both phases, before and after milling process.

there is a little NeH related absorption peaks. The samples show absorption peaks in the region of 1000 to 400 cm^{-1} which correspond to stretching and bending vibrations of metaleoxygen characteristic bonds including the signals at 500 and 600 cm^{-1} . Another broad vibration band at 540 cm^{-1} is due to interaction of oxygen atom with three metal atoms vs (Oe_3Mo) [22].

The ammonia presence in the synthesized materials was determined by IR and this results is in accordance with the thermogravimetric, where can be notice the endothermic and exothermic peaks, this positions were labelled in Fig. 6a. By TGA and IR was determine more quantity of ammonia in the hexagonal phase.

3.6. Change in the optical properties

Employing the Kubelka-Munk formalism obtained from the diffuse reflectance spectra, it was determined the band gap (E_g) values [23]. Fig. 7 shows the extrapolation used to obtained E_g from the $F(R) hv^{1/2}$ vs $h\nu$ (eV) plot. The highest band gap energy value (3.01 eV) belong to as synthesized orthorhombic phase,

followed by the hexagonal phase without milling (2.96 eV). The lowest determined value is 2.75 eV for the orthorhombic sample after a 6 h milling, the values are shown in Table 4. According to the milling time, nanometric particles show a slight decrease of band gap value.

3.7. CASTEP simulation

In order to analyse the performance of the optical properties, a partial density of states (PDOS) simulation was carried out. With this purpose, the Accelrys Material Studio software with the CASTEP code was used [24]. This functional theoretical method to generate the density of states is fast and efficient because it uses valid wave plane type in order to assess the properties of periodic systems (crystals). In the CASTEP, the Perdew-Burke-Emzerhof (PBE) functionals were used in the generalized gradient approximation (GGA) in order to assess the correlation and exchange energies [25]. In our case, to carry out the simulation, the lattice parameters were obtained previously by XRD pattern refinement

Table 4
Band gap energy comparison between experimentally and simulation values, include from reference.

Sample	Band Gap (eV)		
	Experimental	Simulate	Reference [21]
OR-00	3.04	2.5	3.15
OR-02	2.80	–	–
OR-06	2.75	2.1	–
OR-10			2.79
HE-00	2.98	2.8	3.01
HE-02	2.87	–	–
HE-06	2.81	2.6	–

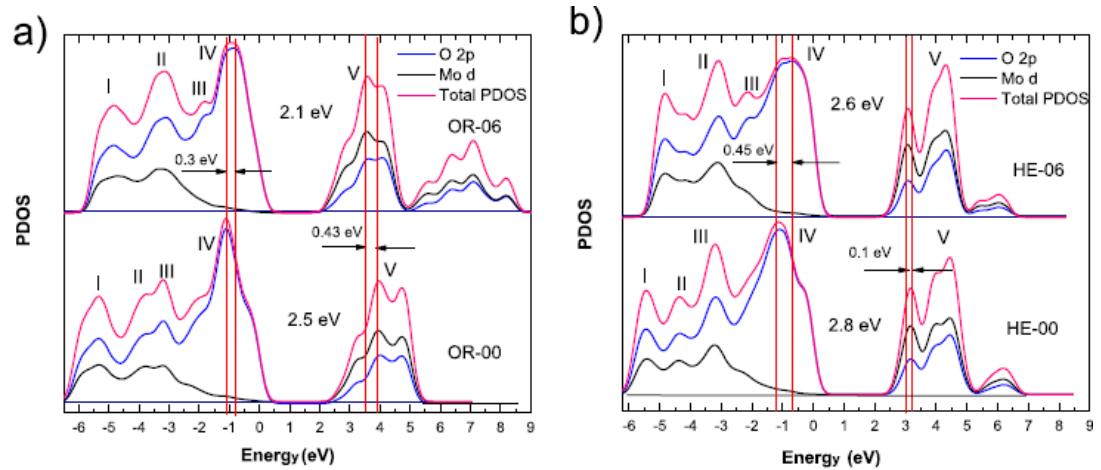


Fig. 8. Partial density graphs for both phases, comparison between without and 6 h milling for a) orthorhombic and b) hexagonal phase.

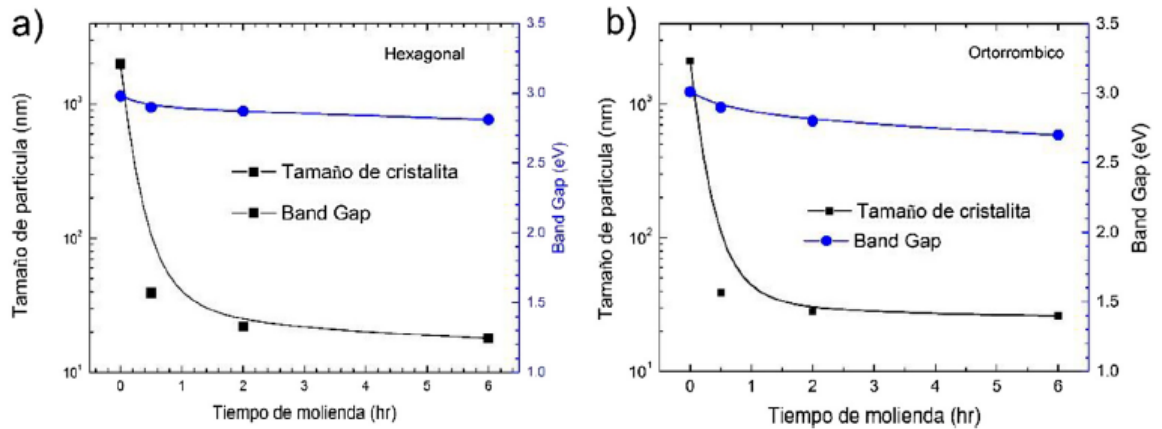


Fig. 9. Particle size and band gap energy variation as a function of milling time. a) orthorhombic and b) hexagonal phase.

Using the Rietveld method (see Table 1). Fig. 8a and b corresponds the results by DFT calculations, which has the same band gap trend determination. The band gap values decrease by the milling time, for orthogon goes from 2.5 to 2.1 eV and for hexagonal goes from 2.8 to 2.6 eV, both after 6 h milling. Additionally, it is observed that the hybridizations of the samples submitted to the milling process show a shift to the right side at 0.3 eV for valence band and shift to the left at 0.43

eV for conduction band, compared with the original material (OR-00). Regarding the conduction band (region V), it is dominated by the d orbital states of the Mo. In the case of hexagonal phase, present the similar behaviour the valence band shift to the right side 0.45 eV and the conduction band to the right side 0.1 eV. These results explain clearly the band gap decrease due to the milling process [26] and they show correlation with the experimental values as observed in Table 4, the values change in the same tendency. It has been reported elsewhere that increasing milling time, the oxygen content is reduced from MoO_{2.929} to MoO_{2.903} after 4 and 6 h, respectively [27]. The slight change in the oxygen content when the materials are submitted to mechanical milling suggests that the Mo⁶⁺ ions are reduced to Mo⁵⁺. At this conditions, it generate an additional energy level above the valence band, thus decreasing the value of the band gap [15,28]. On the other hand, that the oxygen vacancies create defect level between the conduction and valence band for α-MoO₃, which results in the reduction of band gap [29]. These oxygen vacancies create a new state at the forbidden energy band zone, therefore decreasing their value when microstrain increase [30].

The tendency to decrease the band gap as a function of the milling time could be due to the changes generated by this process itself. Fig. 9 shows the band gap and the particle size variation as a

Table 5
Specific surface area before and after milling, include from reference.

Sample	Surface area m ² /gr		Reference 17 m ² /gr
	BET method	Calculated	
OR-00	0.8	5	—
OR-02	33	36	—
OR-06	46	45	—
OR-10	—	—	32
HE-00	0	0.2	—
HE-02	23	30	—
HE-06	32	58	—

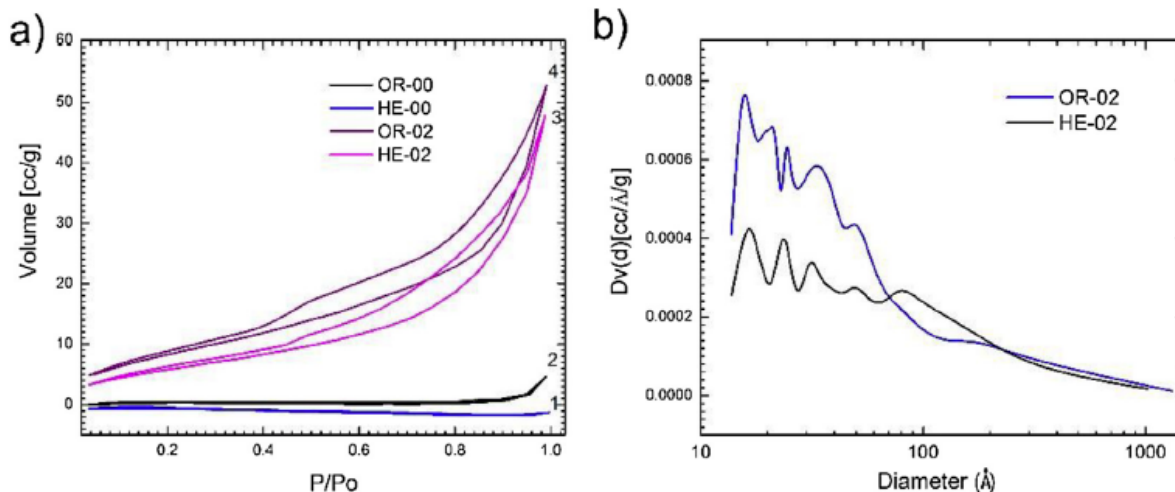


Fig. 10. Nitrogen adsorption-desorption isotherms for a) as synthesized particles (curves 1 and 2) and after 2 h milling (curves 3 and 4), b) pore volume size distributions for OR-02 and HE-02.

Function of the milling time. Both crystallographic phases show the same tendency to decrease drastically the particle size: after 30 min milling, the particles size decrease to 40 nm. Regarding the band gap, there is an initial decrease, then the values were remain without change.

3.8. Changes in a specific surface area

Due to the HEMM process, it was necessary evaluate the effective increase of the surface area as function of the milling time. The particles surface area, before milling is minimum, as it was determine by BET (Table 5). When the materials are submitted to 6 h of milling, the values for the orthorhombic and hexagonal phases were 46 and 32 m²/g, respectively. In order to corroborate these experimental

values, a theoretical calculation was done taking into account the following considerations: considering that the particles obtained by milling possess approximately a spherical shape with sizes reported in Table 3. The volume in cm^3 is calculated for each particle ($V = 4\pi r^3/3$), subsequently using the density values of the orthorhombic and hexagonal phases (4.7 and 3.9 g/cm^3) the mass is calculated for each particle ($M = DV$). Additionally, the surface area of each particle is calculated in m^2 ($A = 4\pi r^2/3$). Finally, the area is divided by the previously calculated mass (A/M), yielding the surface area. The values are reported in Table 5 in comparison with the experimental values. The N_2 adsorption isotherms for materials without milling is shown in Fig. 10a curves 1 and 2 which belongs to type II, they are not present surface area [31]. For Material with 2 h milling, curve 3 and 4 belong to isotherm type IV, which present mesoporosity. The Fig. 10b shows, the pore volume-size distributions, the values goes from 20 nm up to microporous, the porous volumen is not significant and it do not present higher influence. The calculated surface area for hexagonal samples are higher. This could be due to a higher formation of agglomerated particles in this phase. In the case of orthorhombic phase, it correlate well with the calculated values, these particles could be more dispersed in relation to the particles from hexagonal ones.

4. Conclusions

MoO_3 was synthesized by a hydrothermal technique yielding its orthorhombic and hexagonal phases, possessing ribbon-like and hexagonal morphologies with micrometric sizes respectively. Employing high energy mechanical milling process for short periods of 30 min it was possible to obtain materials with 40 nm particles

size. Considerably increasing the materials surface area for new technologic applications in which the surface area is crucial, such as catalysis. The material's band gap tends to decrease, enabling applications close to the visible solar spectrum. Chemical synthesized materials by short time mechanical milling allows the possibility to obtain nanometric size materials with enhanced surface and optical properties.

Acknowledgements

The authors give thanks to the Centro de Investigación en Materiales Avanzados, Laboratorio Nacional de Nanotecnología (NanoTECH). M. Santos-Beltran is supported by CONACYT-México PhD student scholarships. They also give thanks to C. E. Ornelas-Gutiérrez, E. Guerrero Lestarjettel, L. de la Torre Sáenz, D. Lardizábal Gutiérrez, W. Antúnez Flores, I. Estrada Guel and R. Domínguez for technical assistance.

References

- [1] Guodong Wei, Weiping Qin, Daisheng Zhang, Guofeng Wang, Ryongjin Kim, Kezhi Zheng, Lili Wang, J. Alloys Compd. 481 (1e2) (29 July 2009) 417e442.
- [2] Praveen Meduri, Ezra Clark, Jeong H. Kim, Ethirajulu Dayalan, Gamini U. Sumanasekera, Mahendra K. Sunkara, Nano Lett. 12 (2012) 1784e1788.
- [3] Chao-Sheng Hsu, Chih-Chieh Chan, Hung-Tai Huang, Chia-Hsiang Peng, Wen-Chia Hsu, Thin Solid Films 516 (2008) 4839e4844.
- [4] Khojier, H. Savaloni, S. Zolghadr, Surf. Sci. 320 (30 November 2014)

315e321.

[5] F. Paraguay-Delgado, M.A. Albiter, R. Huirache-Acu~na, Y. Verde, G. Alonso-Nu~nez, *Nanosci. Nanotechnol.* 7 (2007) 1e7.

[6] Winny Dong, Bruce Dunn, *J. Non Crystalline Solids* 225 (1998) 135e140.

[7] Anukorn Phuruangrat, Dong Jin Ham, Somchai Thongtem, Jae Sung Lee, *J Electrochem. Commun.* 11 (2009) 1740e1743.

[8] N.A. Dhas, K.S. Suslick, *J. Am. Chem. Soc.* 127 (2005) 2368.

[9] Xianzhong Zeng, Xia Zhang, Min Yang, Yanxing Qi, *A. Mater. Lett.* 112 (2013) 87e89.

[10] Tayier Yunusi, Chao Yang, Wanling Cai, Feng Xiao, Jide Wang, Xintai Su, *J. Nanoparticle Res.* 12 (5) (2010) 1889e1896.

[11] Sylvio Indris, Roger Amade, Paul Heitjans, Mina Finger, Andreas Haeger, Diethard Hesse, Wolfgang Gru1nert, Alexander Bo1rger, Klaus Dieter Becker, *J. Phys. Chem. B* 109 (49) (2005) 23274e23278.

[12] V.V. Sidorchuk, S.V. Khalameida, V.A. Zazhigalov, *Inorg. Mater.* 45 (11) (2009).

[13] L.V. Bogutskaya, S.V. Khalameida, V.A. Zazhigalov, *Theor. Exp. Chem.* 35 (4)(1999).

[14] P. Armstrong, C. Knieke, M. Mackovic, G. Frank, A. Hartmaier, *Acta Mater.* 57 (2009), 3060e3307.

- [15] V.V. Molchanov, R.A. Buyanov, Russ. Chem. Rev. 69 (5) (2000) 435e450.
- [16] Liqiang Mai, Bin Hu, Wen Chen, Yanyuan Qi, Changshi Lao, Rusen Yang, Ying Dai, Zhong Lin Wang, Adv. Mater. 19 (2007) 3712e3716.
- [17] W. Li, F. Cheng, Z. Tao, J. Chen, J. Phys. Chem. B 110 (2006) 119e124.
- [18] G. Vitalea, M.L. Frauwallner, E. Hernandez, C.E. Scott, P. Pereira-Almao, Appl. Catal. A: General 400 (2011) 221e229.
- [19] G. Mestl, B. Herzog, R. Schloegl, H. Knozinger, Langmuir 11 (1996) 3027e3034